Available online at www.sciencedirect.com
ScienceDirect
Journal of Computational Physics 226 (2007) 2206–2228
JOURNAL OF COMPUTATIONAL PHYSICS
www.elsevier.com/locate/jcp

Simulation of flexible filaments in a uniform flow by the immersed boundary method

Wei-Xi Huang, Soo Jai Shin, Hyung Jin Sung *

Department of Mechanical Engineering, Korea Advanced Institute of Science and Technology, 373-1, Guseong-dong, Yuseong-gu, Daejeon 305-701, Republic of Korea

Received 19 February 2007; received in revised form 27 June 2007; accepted 4 July 2007
Available online 21 July 2007

Abstract

An improved version of the immersed boundary (IB) method is developed for simulating flexible filaments in a uniform flow. The proposed IB method is based on an efficient Navier–Stokes solver adopting the fractional step method and a staggered Cartesian grid system. The fluid motion defined on an Eulerian grid and the filament motion defined on a Lagrangian grid are independently solved and their interaction force is explicitly calculated using a feedback law. A direct numerical method is developed to calculate the filament motion under the constraint of inextensibility. When applied to the case of a swinging filament analogous to a rope pendulum, the proposed method gave results very similar to those of the analytical solution derived using the perturbation method. For a flexible filament flapping in a uniform flow, the mechanism by which small vortex processions are produced was investigated. The bistable property of the system was observed by altering the filament length, and the effects of the boundary condition at the fixed end (simply supported or clamped) were studied. For two side-by-side filaments in a uniform flow, both in-phase flapping and out-of-phase flapping were reproduced in the present simulations. A repulsive force was included in the formulation to handle collisions between the free ends of side-by-side filaments undergoing out-of-phase flapping.

Keywords: Immersed boundary method; Fluid-structure interaction; Flexible filament; Inextensibility; Feedback forcing

1. Introduction

Systems involving flexible bodies interacting with a surrounding fluid flow are commonplace – for example flapping flags and swimming fishes – and are becoming increasingly prevalent in biological engineering applications. Such phenomena are challenging to model numerically on account of their complex geometries and freely moving boundaries, which give rise to complicated fluid dynamics. In these systems, the flexible body acts on the surrounding fluid, forcing it to move with the moving boundary. On the other hand, the fluid exerts forces on the flexible body through pressure differences and viscous shear stresses. Together, these interactions

* Corresponding author. Tel.: +82 42 869 3027; fax: +82 42 869 5027.
E-mail address: hjsung@kaist.ac.kr (H.J. Sung).

0021-9991/$ - see front matter © 2007 Elsevier Inc. All rights reserved.
doi:10.1016/j.jcp.2007.07.002

between the fluid and the flexible-body can give rise to self-sustained oscillations such as the flapping of a flag [1–5].

Zhang et al. [1] visualized the motion of flexible filaments in a flowing soap film as a two-dimensional model of the flag-in-the-wind problem. They found two distinct stable states for a single filament (see Fig. 1(a)): the stretched-straight state and the self-sustained flapping state. For two side-by-side filaments (see Fig. 1(b)), four dynamical states were observed, among which in-phase flapping and out-of-phase flapping can be selected by altering the interfilament distance. This experiment inspired numerical simulations on the interaction between flexible filaments and viscous fluid flow. Peskin and co-workers [6–8] simulated both a filament and two side-by-side filaments for comparison with Zhang et al.'s experiment using a new version of the immersed boundary (IB) method, which can handle the mass of the filament. They found that the filament mass plays a significant role in the dynamics of flapping. Yu [9] extended the distributed Lagrangian multiplier/fictitious domain formulation [10] to deal with the interactions between a fluid and a flexible body. Farnell et al. [11] developed another method, in which the motion of a filament is formulated by Lagrange mechanics by regarding the filament as an '*N*-tuple pendulum' and the hydrodynamic force acting on the filament was approximated by the pressure difference across the filament. Systems of flexible fibers suspended in viscous flows, which are important in the paper and pulp industries, were simulated numerically by Tornberg and Shelley [12] and Qi [13]. In fact, previous results show that even a filament alone without ambient fluid flow (also termed as a chain or string when the bending rigidity is neglected) gives rise to complex dynamics. Many interesting studies have been made of filament dynamics, including theoretical, numerical and experimental works [14–16].

Recently, the IB method for simulating interactions between fluids and structures has received much attention due to its greatly simplified grid generation requirements [17]. Specifically, by introducing a momentum forcing into the Navier–Stokes (N–S) equations to mimic the no-slip condition, the N–S solvers based on a Cartesian grid system can be easily applied to complex flow geometries without the need for a boundary-conforming grid. More importantly, it is not necessary to regenerate or deform the grid to account for moving boundaries. The IB method developed by Peskin [18] turns out to be an efficient method for simulating fluid–structure interactions, especially the interactions between fluids and flexible bodies, which are typically encountered in biofluid mechanics [19]. The fluid motion is described by Eulerian variables defined on a fixed Cartesian mesh, while the IB motion is described by Lagrangian variables defined on a freely moving mesh. The Eulerian and Lagrangian variables are connected by a smoothed approximation of the Dirac delta function. The Eulerian velocities are interpolated on the IB and the Lagrangian forcing calculated on the IB spreads to the Eulerian grid. For immersed elastic boundaries, the Lagrangian forcing is just the elastic force, which can be derived by the principle of virtual work or a constitutive law such as Hooke's law [19]. For rigid boundaries, however, the constitutive law for elastic boundaries is not generally well posed. Hence, a feedback control of the velocity along rigid boundaries was proposed by Goldstein et al. [20] and others [21,22]. Lai and Peskin [23] used a stiff spring restoring force to force the IB to attach to the equilibrium or prescribed positions. A difference between the scheme of Goldstein and that of Lai and Peskin is that the boundary points are exactly prescribed in the former scheme, but allowed to move slightly from their equilibrium positions in the latter.

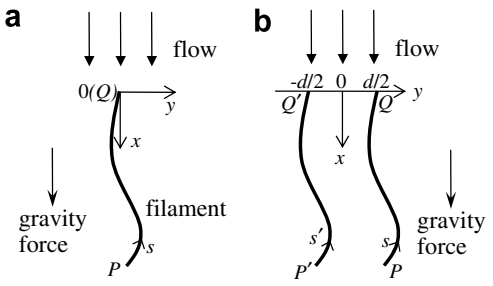

Fig. 1. Schematic diagram of the computational configuration and coordinate systems: (a) a filament in a uniform flow; (b) two side-by-side filaments in a uniform flow.

Peskin [19] showed that the equations of motion of an incompressible elastic material can be written in the same form as those of the incompressible fluid; hence, the governing equations of the whole computational domain are the N–S equations with a momentum forcing, which are non-zero only near the IB. To achieve massless (or neutrally buoyant) elastic boundaries, the only modification of the original N–S solver required is the addition of the momentum forcing to the right hand side of the momentum equations. However, more complications are encountered when the boundaries have mass since the density is not uniform across the whole computational domain. Moreover, the efficient fast Fourier transformation (FFT) method is no longer applicable for this system. Zhu and Peskin [6], in work aimed at simulating flexible filaments in a fluid to compare the simulated behavior with the results of Zhang et al.'s experiment [1], handled this problem by spreading the mass of the IB to the near Eulerian grid points in the same manner as the momentum forcing. The multigrid method was used to solve the discretized equations, and iterations were needed at each time step, which substantially increased the computation time. Kim and Peskin [8] proposed a different formulation referred to as the penalty IB (pIB) method in order to retain the use of the FFT. In the pIB method, the mass is added by introducing a twin boundary with the needed mass that does not directly interact with the fluid but rather is connected to its twin massless boundary by a stiff spring. In both papers, they treated the filament to be elastic and used a constant stretching coefficient. To approximate the inextensibility of the filament, a large stretching coefficient should be chosen in computation.

In the present study, an improved version of the IB method is proposed to handle the mass of a filament. In the proposed method, fluid motion is governed by the N–S equations and a momentum forcing is added to induce the fluid to move at the same velocity as the IB. A flexible inextensible filament model is described by another set of equations with an additional momentum forcing which is the result of the interaction with the surrounding fluid. The Eulerian fluid motion and the Lagrangian IB motion are solved independently and their interaction force is calculated explicitly using a feedback law [20]. The primary aim is to efficiently simulate the interaction between flexible filaments and a viscous fluid flow. Although some previous studies of such systems have been made using the IB method [6–8] and other methods [9,11], many issues remain unresolved. The inextensibility condition of the filament was not strictly satisfied in the IB method used in these previous works. Although a stable flapping motion was obtained, the small vortex procession observed experimentally was not reproduced in the numerical studies. Moreover, the effect of the boundary condition at the fixed end of the filament (simply supported or clamped) was not fully explored. Finally, collisions between adjacent filaments were not considered. All of these issues are resolved in the present method. In addition, the motion of a single filament without ambient fluid under a gravitational force, analogous to a rope pendulum, is simulated and its analytical solution is derived for validation.

2. Problem formulation

A schematic diagram of the computational configuration and coordinate systems is shown in Fig. 1. In Fig. 1(a), a flexible filament with one end fixed and the other free is subjected to a uniform flow. The fixed end of the filament coincides with the origin of the Eulerian coordinate system. For convenience, the Lagrangian coordinate (s) along the filament starts at the free end P and ends at the fixed end Q. It should be pointed out that, for the numerical simulation, it is equivalent for the Lagrangian coordinate to start at P or to start at Q. The direction of the gravity force is denoted in Fig. 1. For the case of two side-by-side filaments, denoted by PQ and $P'Q'$ in Fig. 1(b), the fixed ends are located at $y = d/2$ and $-d/2$, respectively. Each filament has its own Lagrangian coordinate system.

The incompressible viscous fluid flow is governed by the N–S equations and the continuity equation

$$\rho_0\left(\frac{\partial \boldsymbol{u}}{\partial t} + \boldsymbol{u}\cdot\nabla\boldsymbol{u}\right) = -\nabla p + \mu\nabla^2\boldsymbol{u} + \boldsymbol{f}, \tag{1}$$

$$\nabla\cdot\boldsymbol{u} = 0, \tag{2}$$

where $\boldsymbol{u} = (u, v)$ is the velocity vector, p is the pressure, ρ_0 is the fluid density, μ is the dynamic viscosity, and $\boldsymbol{f} = (f_x, f_y)$ is the momentum forcing applied to enforce the no-slip boundary condition along the IB.

The flexible filaments used in the present study are massive and inextensible. The governing equations for a filament are written in a Lagrangian form. The motion equations are

$$\rho_1 \frac{\partial^2 \boldsymbol{X}}{\partial t^2} = \frac{\partial}{\partial s}\left(T\frac{\partial \boldsymbol{X}}{\partial s}\right) - \frac{\partial^2}{\partial s^2}\left(\gamma \frac{\partial^2 \boldsymbol{X}}{\partial s^2}\right) + \rho_1 \boldsymbol{g} - \boldsymbol{F} + \boldsymbol{F}_c, \tag{3}$$

where s is the arclength, $\boldsymbol{X} = (X(s,t), Y(s,t))$ is the position, T is the tension force along the filament axis, γ is the bending rigidity, $\boldsymbol{F}$ is the Lagrangian forcing exerted on the filament by the surrounding fluid, and $\boldsymbol{F}_c$ denotes the repulsive force between adjacent filaments in the case of side-by-side filaments. In Eq. (3), ρ_1 denotes the density difference between the filament and the surrounding fluid [9,24]. Since Eq. (3) is one-dimensional in space, the actual filament line density is $\rho_1 + \rho_0 A$, where A denotes the sectional area of the filament. We can see that $\rho_1 = 0$ represents the neutrally buoyant case. The inextensibility condition [12,14,16] is expressed by

$$\frac{\partial \boldsymbol{X}}{\partial s} \cdot \frac{\partial \boldsymbol{X}}{\partial s} = 1. \tag{4}$$

Eqs. (1)–(4) can be non-dimensionalized by introducing the following characteristic scales: the reference filament length L_r for length, the far-field velocity U_∞ for velocity, L_r/U_∞ for time, $\rho_0 U_\infty^2$ for pressure p, $\rho_0 U_\infty^2/L_r$ for the momentum forcing f, $\rho_1 U_\infty^2/L_r$ for the Lagrangian forcing $\boldsymbol{F}$ and the repulsive force $\boldsymbol{F}_c$, $\rho_1 U_\infty^2$ for the tension force T, and $\rho_1 U_\infty^2 L_r^2$ for the bending rigidity γ. For convenience, in the following, the dimensionless quantities are written in the same form as their dimensional counterparts. Eqs. (1) and (3) then become, respectively,

$$\frac{\partial \boldsymbol{u}}{\partial t} + \boldsymbol{u}\cdot\nabla\boldsymbol{u} = -\nabla p + \frac{1}{Re}\nabla^2 \boldsymbol{u} + \boldsymbol{f}, \tag{5}$$

$$\frac{\partial^2 \boldsymbol{X}}{\partial t^2} = \frac{\partial}{\partial s}\left(T\frac{\partial \boldsymbol{X}}{\partial s}\right) - \frac{\partial^2}{\partial s^2}\left(\gamma \frac{\partial^2 \boldsymbol{X}}{\partial s^2}\right) + Fr\frac{\boldsymbol{g}}{g} - \boldsymbol{F} + \boldsymbol{F}_c, \tag{6}$$

where $Re = \rho_0 U_\infty L_r/\mu$, $Fr = gL_r/U_\infty^2$, and $g = |\boldsymbol{g}|$. Eqs. (2) and (4) keep the same forms after non-dimensionalization. Note that different characteristic densities, ρ_0 and ρ_1, are used for Eqs. (1) and (3), respectively. This difference should be accounted for when transforming between the Eulerian and Lagrangian forcings. For comparison, the actual filament length L (after scaling with the reference value L_r) may be set to be different from 1.

In the present study, the tension force T is determined by the constraint of inextensibility and is a function of s and t, while the bending rigidity γ is assumed to be constant. From Eqs. (4) and (6), the Poisson equation for T is derived as

$$\frac{\partial \boldsymbol{X}}{\partial s}\cdot\frac{\partial^2}{\partial s^2}\left(T\frac{\partial \boldsymbol{X}}{\partial s}\right) = \frac{1}{2}\frac{\partial^2}{\partial t^2}\left(\frac{\partial \boldsymbol{X}}{\partial s}\cdot\frac{\partial \boldsymbol{X}}{\partial s}\right) - \frac{\partial^2 \boldsymbol{X}}{\partial t\,\partial s}\cdot\frac{\partial^2 \boldsymbol{X}}{\partial t\,\partial s} - \frac{\partial \boldsymbol{X}}{\partial s}\cdot\frac{\partial}{\partial s}(\boldsymbol{F}_b + \boldsymbol{F}_c - \boldsymbol{F}), \tag{7}$$

where $\boldsymbol{F}_b = -\frac{\partial^2}{\partial s^2}(\gamma \partial^2 \boldsymbol{X}/\partial s^2)$ denotes the bending force. The first term on the right hand side of Eq. (7) is zero theoretically. However, numerical errors of the inextensibility constraint are introduced in the computation and will not be corrected if this term is dropped, as will be explained in detail in the next section. At the free end ($s = 0$), we have

$$T = 0, \quad \frac{\partial^2 \boldsymbol{X}}{\partial s^2} = (0,0), \quad \frac{\partial^3 \boldsymbol{X}}{\partial s^3} = (0,0). \tag{8}$$

At the fixed end ($s = L$), two types of boundary conditions are considered. One is the simply supported condition (denoted *BC1* hereafter),

$$\boldsymbol{X} = \boldsymbol{X}_O, \quad \frac{\partial^2 \boldsymbol{X}}{\partial s^2} = (0,0). \tag{9}$$

The other is the clamped or build-in supported condition (*BC2*),

$$\boldsymbol{X} = \boldsymbol{X}_O, \quad \frac{\partial \boldsymbol{X}}{\partial s} = (-1,0). \tag{10}$$

As shown in Fig. 1, X_O is located at $(0,0)$ for a single filament, while $\boldsymbol{X}_O = (0, d/2)$ and $(0, -d/2)$ for two side-by-side filaments, respectively.

The interaction force between the fluid and the IB can be calculated by the feedback law [20]

$$\boldsymbol{F} = \alpha \int_0^t (\boldsymbol{U}_{ib} - \boldsymbol{U}) \mathrm{d}t' + \beta(\boldsymbol{U}_{ib} - \boldsymbol{U}), \tag{11}$$

where α and β are large negative free constants, $\boldsymbol{U}_{ib}$ is the fluid velocity obtained by interpolation at the IB, and U is the velocity of the filament expressed by $\boldsymbol{U} = \mathrm{d}\boldsymbol{X}/\mathrm{d}t$. Eq. (11) implies that the adjacent fluid points are linked with the IB by a set of identical stiff springs with damping.

The transformation between the Eulerian and Lagrangian variables can be realized by the Dirac delta function [19]. The interpolation of velocity is expressed as

$$\boldsymbol{U}_{ib}(s,t) = \int_\Omega \boldsymbol{u}(\boldsymbol{x},t)\delta(\boldsymbol{X}(s,t) - \boldsymbol{x})\mathrm{d}\boldsymbol{x}. \tag{12}$$

Spreading of the Lagrangian forcing to the nearby grid points is expressed as

$$\boldsymbol{f}(\boldsymbol{x},t) = \rho \int_\Gamma \boldsymbol{F}(s,t)\delta(x - \boldsymbol{X}(s,t))\mathrm{d}s, \tag{13}$$

where $\rho = \rho_1/(\rho_0 L_r)$ comes from non-dimensionalization. In Eq. (13), the Dirac delta function is two-dimensional but there is only one integral $\mathrm{d}s$. The present definition of ρ becomes $\rho = \rho_1/(\rho_0 A)$ if we use the integral $\mathrm{d}V = (A/L_r)\mathrm{d}s$ instead of $\mathrm{d}s$. However, since the sectional area A is not definitely defined, $\rho = \rho_1/(\rho_0 L_r)$ is used in the present study [25]. The combination of Eqs. (11) and (13) means that the velocities at the nearby grid points are forced to move with the IB. The jump conditions in fluid stresses across the IB can be derived from Eqs. (1) and (13) [26]. Peskin and co-workers [6–8] used a different formulation, in which the filament is approximated by a band of delta function and the stretching and bending forces are spread out the nearby grid points. In the present formulation, the motion of the IB can be solved independently and the inextensibility condition can be satisfied.

In the present study, a strategy is introduced for handling collisions between two side-by-side filaments flapping out of phase in a uniform flow. Due to the fluid lubrication, the two filaments do not actually collide but rather interact repulsively via the intervening fluid when they are in close proximity. In the numerical simulation, an artificial repulsive force is activated at close range, as proposed by Glowinski et al. [10]. For flexible filaments, this short-range repulsive force can be formulated using the Dirac delta function

$$\boldsymbol{F}_c(s,t) = \int_0^L \delta(\boldsymbol{X}(s,t) - \boldsymbol{X}'(s',t)) \frac{\boldsymbol{X} - \boldsymbol{X}'}{|\boldsymbol{X} - \boldsymbol{X}'|} \mathrm{d}s', \tag{14}$$

where $\boldsymbol{X}(s,t)$ and $\boldsymbol{X}'(s',t)$ are the position vectors along the two filaments, respectively. After discretization, the forcing range is the support of the smoothed approximation of the Dirac delta function.

3. Numerical method

3.1. Discretization of the filament governing equations

3.1.1. The tension and bending forces

A staggered grid is used in the Lagrangian coordinate system, as shown in Fig. 2, with the tension force defined on the interfaces and the other variables defined on the nodes. The indices start from the free end ($i = 0$) and end at the fixed end ($i = N$). Let D_s, D_{ss} and D_{sss} denote the difference approximation to the

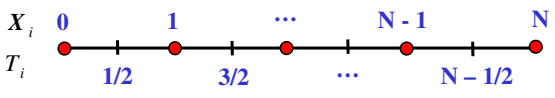

Fig. 2. Schematic diagram of the Lagrangian coordinate system for a flexible filament.

first-, second- and third-order derivatives of the arclength s, respectively. Specifically, for an arbitrary variable ϕ,

$$D_s^0\phi = (\phi(s+\Delta s/2) - \phi(s-\Delta s/2))/\Delta s, \tag{15}$$

$$D_s^+\phi = (\phi(s+\Delta s) - \phi(s))/\Delta s, \tag{16}$$

$$D_s^-\phi = (\phi(s) - \phi(s-\Delta s))/\Delta s \tag{17}$$

denote the center, downwind and upwind difference approximations, respectively. Thus, the second-order central difference approximation is expressed as

$$D_s^+D_s^-\phi = (\phi(s+\Delta s) - 2\phi(s) + \phi(s-\Delta s))/\Delta s^2. \tag{18}$$

The same rules apply for the time t.

The tension force term in Eq. (6) is discretized as

$$[D_s(TD_s\boldsymbol{X})]_i = [D_s^0(TD_s^0\boldsymbol{X})]_i = \frac{T_{i+1/2}(D_s^0\boldsymbol{X})_{i+1/2} - T_{i-1/2}(D_s^0\boldsymbol{X})_{i-1/2}}{\Delta s}, \quad i = 1,2,\ldots,N-1 \tag{19}$$

and the bending force term is discretized as

$$(\boldsymbol{F}_b)_i = -[D_s^+D_s^-(\gamma D_{ss}\boldsymbol{X})]_i = -\gamma\frac{(D_{ss}\boldsymbol{X})_{i+1} - 2(D_{ss}\boldsymbol{X})_i + (D_{ss}\boldsymbol{X})_{i-1}}{\Delta s^2}, \quad i = 1,2,\ldots,N-1, \tag{20}$$

where

$$(D_{ss}\boldsymbol{X})_i = \begin{cases} \boldsymbol{0}, & i = 0, \\ (D_s^+D_s^-X)_i, & i = 1,2,\ldots,N-1, \end{cases} \tag{21}$$

and two boundary condition types (Eqs. (9) and (10)) at the fixed end are accounted for

$$(D_{ss}\boldsymbol{X})_N = \begin{cases} 0, & \text{simply supported}, \\ [(-1,0) - (D_s^0\boldsymbol{X})_{N-1/2}]/0.5\Delta s, & \text{clamped}, \end{cases} \tag{22}$$

where $(D_s\boldsymbol{X})_N = (-1,0)$ is used according to Eq. (10).

At the free end ($i = 0$), the tension and bending force terms in Eq. (6) are discretized using Eq. (8), yielding

$$[D_s(TD_s\boldsymbol{X})]_0 = \frac{(TD_s\boldsymbol{X})_{1/2} - (TD_s\boldsymbol{X})_0}{\Delta s/2} = \frac{T_{1/2}(D_s^0\boldsymbol{X})_{1/2}}{\Delta s/2}, \tag{23}$$

$$(\boldsymbol{F}_b)_0 = -\gamma[D_s^+(D_{sss}\boldsymbol{X})]_0 = -\gamma\frac{(D_{sss}\boldsymbol{X})_1 - (D_{sss}\boldsymbol{X})_0}{\Delta s} = -\gamma\frac{(D_s^+D_s^-\boldsymbol{X})_2 - (D_s^+D_s^-\boldsymbol{X})_1}{\Delta s^2}. \tag{24}$$

At the fixed end ($i = N$), we have $\partial^2\boldsymbol{X}/\partial t^2 = 0$ and $\boldsymbol{F}_c = 0$, and hence

$$[D_s(TD_s\boldsymbol{X})]_N - [D_{ss}(\gamma D_{ss}\boldsymbol{X})]_N = \left(\boldsymbol{F} - Fr\frac{\rho g}{g}\right)_N. \tag{25}$$

3.1.2. Time marching scheme

Now, the discretization of Eq. (6) can be summarized as

$$\frac{\boldsymbol{X}_i^{n+1} - 2\boldsymbol{X}_i^n + \boldsymbol{X}_i^{n-1}}{\Delta t^2} = [D_s(T^{n+1/2}D_s\boldsymbol{X}^{n+1})]_i + (\boldsymbol{F}_b^*)_i + Fr\frac{\mathbf{g}}{g} - \boldsymbol{F}_i^n + (\boldsymbol{F}_c)_i^*, \quad i = 0,1,2,\ldots,N, \tag{26}$$

where the superscript n denotes the nth time step, Δt denotes the time increment, and the boundary conditions (Eqs. (23)–(25)) should be accounted for at $i = 0$ and $i = N$. At the fixed end, Eq. (25) is equivalent to $(\boldsymbol{X}_N^{n+1} - 2\boldsymbol{X}_N^n + \boldsymbol{X}_N^{n-1})/\Delta t^2 = \boldsymbol{0}$. The bending force terms $\boldsymbol{F}_b^*$ and $\boldsymbol{F}_c^*$ are explicitly calculated in the form of $\boldsymbol{F}_b^* = \boldsymbol{F}_b(2\boldsymbol{X}^n - \boldsymbol{X}^{n-1})$ and $\boldsymbol{F}_c^* = \boldsymbol{F}_c(2\boldsymbol{X}^n - \boldsymbol{X}^{n-1})$, respectively. The tension force term is implicitly treated, while $T^{n+1/2}$ is the tension force at the intermediate time step and is obtained by solving Eq. (7).

The first term on the right hand side of Eq. (7) is discretized as

$$\frac{1}{2}D_t^+D_t^-(D_s^0\boldsymbol{X}^n\cdot D_s^0\boldsymbol{X}^n)=\frac{1-2(D_s^0\boldsymbol{X}\cdot D_s^0\boldsymbol{X})^n+(D_s^0\boldsymbol{X}\cdot D_s^0\boldsymbol{X})^{n-1}}{2\Delta t^2}. \tag{27}$$

In the above equation, we used the inextensibility condition $(D_s\boldsymbol{X}\cdot D_s\boldsymbol{X})^{n+1}=1$. The numerical errors introduced in previous time steps, i.e. $(D_s\boldsymbol{X}\cdot D_s\boldsymbol{X})^n$ and $(D_s\boldsymbol{X}\cdot D_s\boldsymbol{X})^{n-1}$, are penalized. The discretized form of Eq. (7) can be written as

$$\begin{aligned}&(D_s^0\boldsymbol{X}^*)_{i+1/2}\cdot[D_s^0(D_s(T^{n+1/2}D_s\boldsymbol{X}^*))]_{i+1/2}\\&\quad=\frac{1}{2}D_t^+D_t^-(D_s^0\boldsymbol{X}^n\cdot D_s^0\boldsymbol{X}^n)_{i+1/2}-(D_s^0\boldsymbol{U}^n\cdot D_s^0\boldsymbol{U}^n)_{i+1/2}-(D_s^0\boldsymbol{X}^*)_{i+1/2}\cdot[D_s^0(\boldsymbol{F}_{\mathrm{b}}^*-\boldsymbol{F}^n+\boldsymbol{F}_{\mathrm{c}}^*)]_{i+1/2},\\&\quad i=0,1,2,\ldots,N-1,\end{aligned} \tag{28}$$

where $\boldsymbol{X}^*=2\boldsymbol{X}^n-\boldsymbol{X}^{n-1}$, which is the solution of Eq. (26) by setting the right hand side to be zero. The discretization of the tension and bending forces (Eqs. (19) and (20)) are applied in Eq. (28), and the boundary conditions (Eqs. (23)–(25)) are applied for $i=0$ and $i=N-1$. Solution of Eq. (28) gives the tension force at the intermediate time step, $T^{n+1/2}$, which is then used as an inextensibility constraint to obtain $\boldsymbol{X}^{n+1}$ from Eq. (26). No iteration is needed for time advancement at each time step. In practice, the inextensibility condition is well satisfied and use of the predicted position $\boldsymbol{X}^*=2\boldsymbol{X}^n-\boldsymbol{X}^{n-1}$ instead of $\boldsymbol{X}^n$ reduces the error further.

3.1.3. The interaction and repulsive forces

In Eqs. (26) and (28), the interaction force term is calculated explicitly, i.e.,

$$\boldsymbol{F}_i^n=\alpha\sum_{j=1}^{n}((\boldsymbol{U}_{ib})_i^j-\boldsymbol{U}_i^j)\mathrm{d}t'+\beta((\boldsymbol{U}_{ib})_i^n-\boldsymbol{U}_i^n),\quad i=0,1,2,\ldots,N, \tag{29}$$

where $\boldsymbol{U}_i^j=(\boldsymbol{X}_i^j-\boldsymbol{X}_i^{j-1})/\Delta t,\ j=1,2,\ldots,n$ and

$$(\boldsymbol{U}_{ib})_i^j=\sum_{\boldsymbol{x}_{ml}\in g_h}\boldsymbol{u}_{ml}^j\delta_h(\boldsymbol{X}_i^j-\boldsymbol{x}_{ml})h^2,\quad i=0,1,2,\ldots,N,\ \ j=1,2,\ldots,n. \tag{30}$$

In the above equation, h denotes the mesh size and, in the present simulations, a mesh of uniform size is distributed around the IB in the x- and y-directions, i.e. $h=\Delta x=\Delta y$. g_h is the support of the smoothed delta function δ_h

$$\delta_h(\boldsymbol{x})=\frac{1}{h^2}\phi\left(\frac{x}{h}\right)\phi\left(\frac{y}{h}\right). \tag{31}$$

In this paper we use the four-point delta function introduced by Peskin [19]

$$\phi(r)=\begin{cases}\frac{1}{8}(3-2|r|+\sqrt{1+4|r|-4r^2}), & 0\leqslant|r|<1,\\ \frac{1}{8}(5-2|r|-\sqrt{-7+12|r|-4r^2}), & 1\leqslant|r|<2,\\ 0, & 2\leqslant|r|.\end{cases} \tag{32}$$

On the other hand, the Lagrangian forcing is spread to the Eulerian grid

$$\boldsymbol{f}_{ml}^{\ n}=\rho\sum_{i=1}^{N}\boldsymbol{F}_i^n\delta_h(\boldsymbol{x}_{ml}-\boldsymbol{X}_i^n)\Delta s\quad\forall\boldsymbol{x}_{ml}\in g_h. \tag{33}$$

The total amount of force is conserved by the above transformation

$$\sum_{x_{ml}\in g_h}\boldsymbol{f}_{ml}^{\ n}h^2=\sum_{i=1}^{N}\rho\boldsymbol{F}_i^n\Delta s. \tag{34}$$

In addition, the short-range repulsive force (Eq. (14)) is discretized as

$$(\boldsymbol{F}_c)_i^* = \sum_{j=1}^{n} \delta_h(\boldsymbol{X}_i^* - \boldsymbol{X}_j'^*) \frac{\boldsymbol{X}_i^* - \boldsymbol{X}_j'^*}{|\boldsymbol{X}_i^* - \boldsymbol{X}_j'^*|} \Delta s, \quad i = 0, 1, 2, \ldots, N. \tag{35}$$

3.2. The flow solver

3.2.1. Fractional step method

The N–S equations are discretized as

$$\frac{\boldsymbol{u}^{n+1} - \boldsymbol{u}^n}{\Delta t} + N\boldsymbol{u}^{n+1} = -Gp^{n+1/2} + \frac{1}{2Re}(L\boldsymbol{u}^{n+1} + L\boldsymbol{u}^n) + \boldsymbol{f}^{\,n}, \tag{36}$$

$$D\boldsymbol{u}^{n+1} = 0, \tag{37}$$

where N, G, L and D are the linearized discrete convective operator, the discrete gradient operator, the discrete Laplacian operator, and the discrete divergence operator, respectively. The N–S equations are solved by the fractional step method on a staggered Cartesian grid. The velocity components and momentum forcing are defined on the staggered grid, whereas the pressure is applied at the centers of cells. Fully implicit time advancement is employed, with the Crank–Nicholson scheme being used for the discretization of the diffusion and convection terms. Decoupling of the velocity and pressure is achieved by block LU decomposition in conjunction with approximate factorization. Details of the approximate factorization can be found in Kim et al. [27]. In summary, it can be written as

$$\frac{\boldsymbol{u}^* - \boldsymbol{u}^n}{\Delta t} + N\boldsymbol{u}^* = -Gp^{n-1/2} + \frac{1}{2Re}(L\boldsymbol{u}^* + L\boldsymbol{u}^n) + \boldsymbol{f}^{\,n}, \tag{38}$$

$$\Delta t DG\delta p = D\boldsymbol{u}^*, \tag{39}$$

$$\boldsymbol{u}^{n+1} = \boldsymbol{u}^* - \Delta t G\delta p, \tag{40}$$

$$p^{n+1/2} = p^{n-1/2} - \delta p, \tag{41}$$

where $\boldsymbol{u}^*$ denotes the intermediate velocity. Due to the implicit treatment of the nonlinear convection terms, further decoupling of the intermediate velocity components is made and finally a system of tridiagonal matrices is formed instead of a large sparse matrix [27]. The momentum equation is then solved directly without iteration, and the computational cost is reduced significantly. The pressure Poisson equation is solved by a direct method using FFT or a multigrid method. The pressure is then used to correct the velocity field to satisfy the continuity equation.

3.2.2. Summary of the numerical algorithm

The general process of the present numerical algorithm for simulating flexible filaments in a uniform flow can be summarized as follows:

(1) At the nth time step, we know the fluid velocity field $\boldsymbol{u}^n$ and the filament positions $\boldsymbol{X}^n$ and $\boldsymbol{X}^{n-1}$. Interpolate the fluid velocity at the IB to obtain $\boldsymbol{U}_{ib}^n$ by Eq. (30), and then calculate the Lagrangian interaction force $\boldsymbol{F}^n$ by Eq. (29).
(2) Spread the Lagrangian interaction force to the Eulerian grid by using Eq. (33). Solve Eqs. (38)–(41) to obtain the updated fluid velocity field and pressure field.
(3) Calculate the tension force at the intermediate time step $T^{n+1/2}$ by Eq. (28). Solve Eq. (26) to obtain the filament position at the new time step $\boldsymbol{X}^{n+1}$. This ends one time step marching.

In the present simulations, the computational domain for fluid–structure interactions is a rectangle, and a uniform flow moves from the top to the bottom of the computational domain, as shown in Fig. 1. Dirichlet boundary conditions ($u = U_\infty$, $v = 0$) are used at the inflow and far-field boundaries, and a convective boundary condition is used at the outflow.

3.2.3. Validation

To validate the present N–S solver in combination with the feedback forcing scheme, we simulated a uniform flow over a transversely oscillating circular cylinder. Since in this system the motion of the IB is prescribed, step (3) of the above numerical procedure is simply substituted by giving the known IB position at the new time step. The cylinder is oscillating harmonically according to

$$y_c(t) = A_m \cos(2\pi f_e t) \tag{42}$$

where y_c is the position of the cylinder center, A_m is the oscillation amplitude, and f_e is the oscillation frequency. The characteristic length L_r is set to be the cylinder diameter D, so the Reynolds number is defined as $Re = \rho_0 U_\infty D/\mu$. The computation is performed at $Re = 185$, $A_m/D = 0.2$ as in Guilmineau and Queutey [28], and two cases, namely $f_e/f_0 = 0.9$ and 1.1, are simulated for comparison, where f_0 is the natural shedding frequency for a stationary cylinder ($f_0 = 0.19$ for $Re = 185$ [28]). The computational domain is $-50D \leqslant x \leqslant 50D$ and $-50D \leqslant y \leqslant 50D$, and the grid size is 513×283 in the streamwise (x) and transverse (y) directions, respectively. Sixty grid points are uniformly distributed inside the cylinder in both the x- and y-directions and the grid is stretched outside of the cylinder. It is well known [20,21] that the time step is restricted by using the free constants α and β in Eq. (29). Lee [22] obtained the precise stability boundaries for several time-advancing schemes. Based on the results of Lee, in this simulation we use $\alpha = -2 \times 10^3$, $\beta = -10$ and $\Delta t = 0.005$ and the maximum CFL number is about 0.5.

Fig. 3 shows the time evolution of the drag and lift coefficients for $f_e/f_0 = 0.9$ and 1.1. For $f_e/f_0 = 0.9$ (Fig. 3(a)), the lift (drag) coefficient varies with time at a single frequency, once the vortex shedding is established. For $f_e/f_0 = 1.1$ (Fig. 3(b)), however, a higher harmonic is seen, which corresponds to the phenomenon of vortex switching [28]. The values of the mean drag coefficient (C_D), the rms drag and lift fluctuation coefficients (C'_D and C'_L, respectively), and the phase angle between C_L and the vertical position of the cylinder (ϕ) are presented in Table 1, which also lists the corresponding values from previous studies for comparison. We can see that the present results agree well with those of Guilmineau and Queutey [28] and Kim and Choi [29].

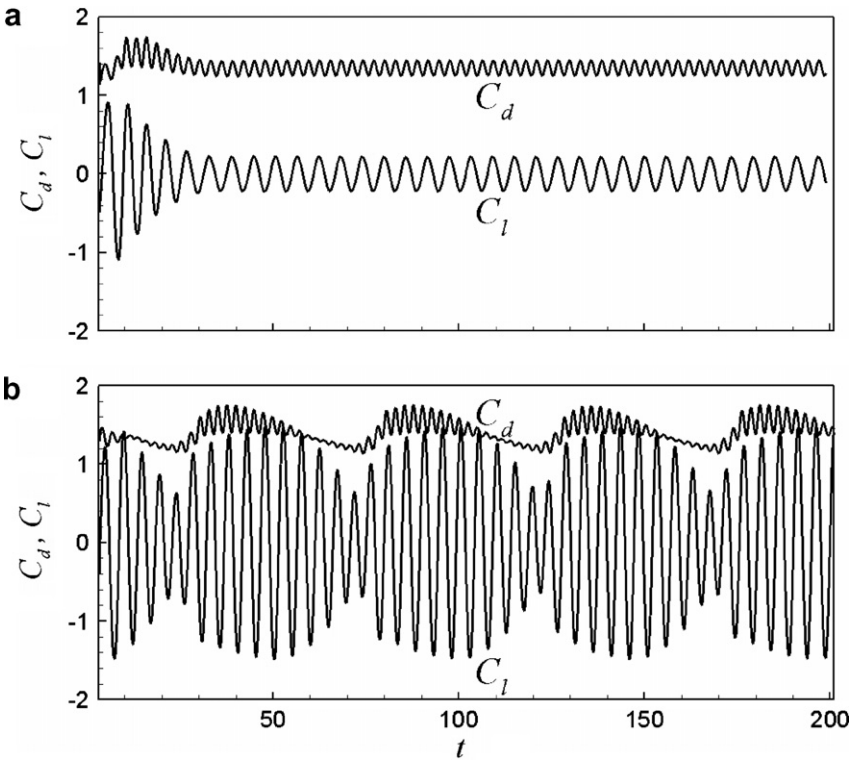

Fig. 3. Time history of drag and lift coefficients at $Re = 185$, $A_e/D = 0.2$ and the values of f_e/f_o equal to: (a) 0.90; (b) 1.10.

Table 1
Comparison of the mean drag coefficient (C_D), the rms drag and lift fluctuation coefficients (C'_D and C'_L, respectively), and the phase angle between C_L and the vertical position of the cylinder (ϕ)

		C_D	C'_D	C'_L	ϕ
$f_e/f_o = 0.9$	Present	1.35	0.068	0.15	126.43
	Guilmineau and Queutey [28]	1.33	0.077	0.19	128.11
	Kim and Choi [29]	1.37	0.078	0.17	124.49
$f_e/f_o = 1.1$	Present	1.41	0.15	0.90	1.26
	Guilmineau and Queutey [28]	1.36	0.15	0.87	0.00
	Kim and Choi [29]	1.40	0.14	0.87	5.31

4. Results and discussion

4.1. A hanging filament without ambient fluid

The motion of a hanging filament without ambient fluid under a gravitational force, which is analogous to a rope pendulum, can be simulated by Eqs. (6) and (7) with the boundary conditions given by Eqs. (8) and (9). Thus steps (1) and (2) of the numerical algorithm are omitted for this problem. The filament is initially held stationary at an angle from the vertical

$$\boldsymbol{X}(s,0) = \boldsymbol{X}_O + (L-s)(\cos k, \sin k), \quad \partial \boldsymbol{X}(s,0)/\partial t = (0,0), \tag{43}$$

where k is a constant, and $\boldsymbol{X}_O = (0,0)$. At $t = 0$, it is released and starts swinging due to the gravity force. Fig. 4 shows a superposition of the filament positions at successive times over half an oscillation period (a time period of 0.8). This time period is marked as A to B in Fig. 5, which shows the time history of the free end position of the filament. In these simulations, we use $L = 1$, $N = 100$, $Fr = 10.0$, and $k = 0.1\pi$, and compare systems with two different bending rigidities: without the bending force ($\gamma = 0$), and with the bending force included ($\gamma = 0.01$). As shown in Fig. 4(a), the filament is totally flexible in the absence of the bending force ($\gamma = 0$), and the free end rolls up obviously at the left side, a feature known as a 'kick' [15]. When the bending

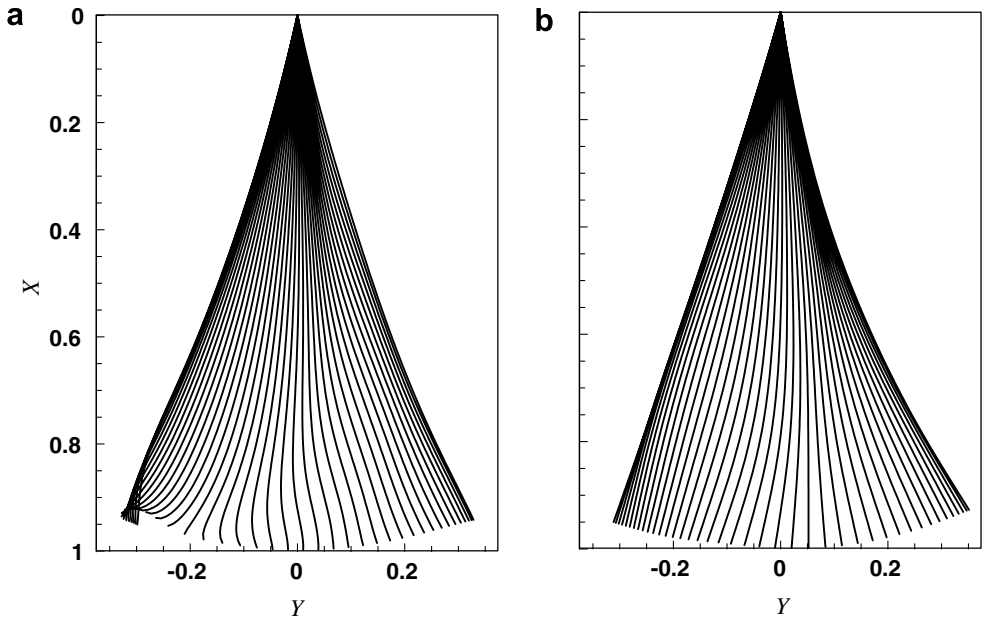

Fig. 4. Superposition of the filament positions (from left to right) at successive times: (a) $\gamma = 0.0$; (b) $\gamma = 0.01$. The time step is 0.02 and the time duration is 0.8.

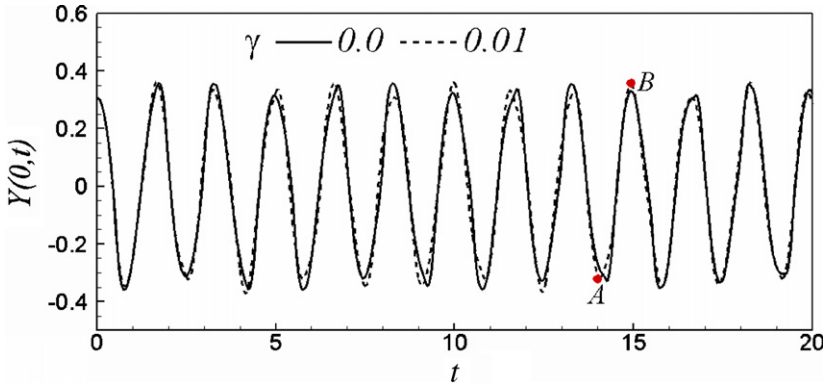

Fig. 5. Time history of the free end position of the filament.

force is included ($\gamma = 0.01$), by contrast, the filament remains straighter during the pendulum motion and no kick is observed (Fig. 4(b)). In Fig. 4(a), a kick is observed on the left side but not the right side. Interestingly, during the whole time history, the kick behavior appears at the right extreme in the following sequence: $-++-++\cdots$, where '+' denotes a kick and '−' denotes no-kick, while the sequence at the left extreme is: $+-++-+\cdots$. Kick behavior is not observed at any time for $\gamma = 0.01$. Despite this difference in kick behavior, however, the time history of the free end position (Fig. 5) shows little difference between the two cases, except at the extremes where the kick behavior occurs.

The filament is inextensible, so it is of interest to monitor the error of the inextensibility constraint introduced during the simulation, which is defined as

$$\varepsilon(t) = \max_{0 \leqslant s \leqslant L} \left| \frac{\partial \boldsymbol{X}}{\partial s} \cdot \frac{\partial \boldsymbol{X}}{\partial s} - 1 \right|, \tag{44}$$

where $|\cdot|$ denotes the absolute value. As shown in Fig. 6, the magnitude of $\varepsilon(t)$ is small, which means that the inextensibility condition is well satisfied. Due to the kick behavior, which causes greater bending of the filament, the error is larger for the $\gamma = 0$ system than for the $\gamma = 0.01$ system.

For the case where the swing amplitude is small and the bending force is neglected, we used the perturbation method to derive the analytical solution in series form (see Appendix). Twenty terms are summed up to approximate the series (Eq. (61)) and the truncation error is less than 10^{-5}. We compared the results obtained using the analytical solution with those from a simulation using $\gamma = 0$, $k = 0.01\pi$ with the other parameters the same as in the simulations described above. As shown in Fig. 7, the free end position of the filament obtained from the analytical solution (Eq. (61)) coincides with the numerical result with the inextensibility condition.

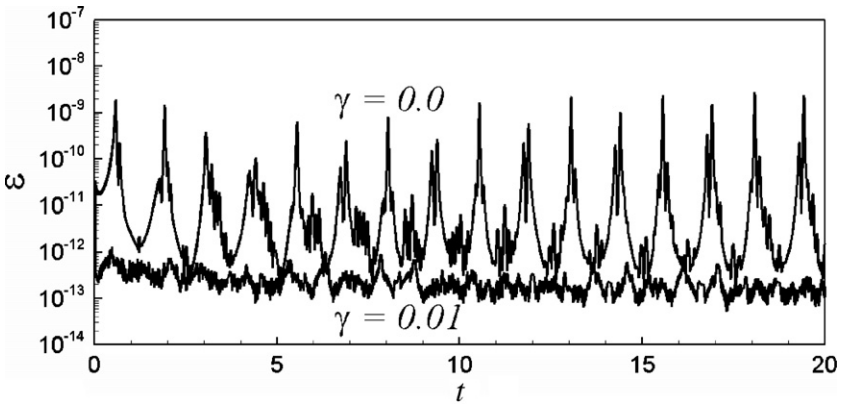

Fig. 6. Time history of the length error of the filament.

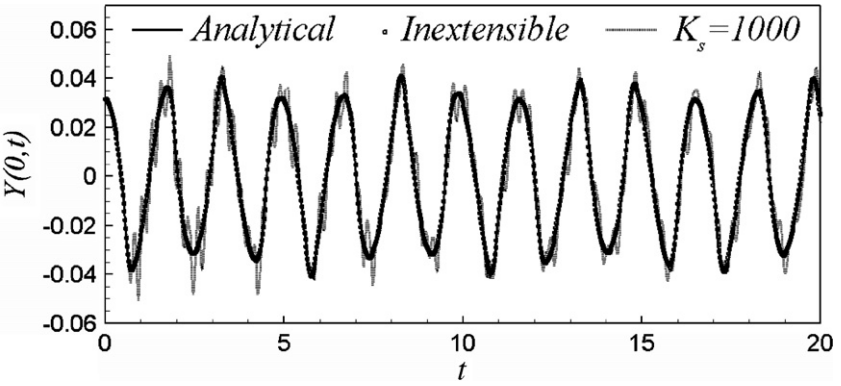

Fig. 7. Comparison of the free end position of the filament between the present simulations and the analytical solution.

We simulated this problem by using a constant filament stretching coefficient (K_S) instead of the inextensibility condition to calculate the tension force, i.e. $T = K_S(|\partial \boldsymbol{X}/\partial s| - 1)$, as in Zhu and Peskin [6]. The tension force term is treated implicitly, while the bending force term is treated explicitly. The result obtained by using $K_S = 1000$, $\gamma = 0$ and $k = 0.01\pi$ is shown in Fig. 7 for comparison. We can see the obvious deviation of the free end position from those of the inextensibility condition and the analytical solution. If we choose a large K_S, the error is reduced but a small time step is required. Table 2 lists the maximum time step, the length error defined in Eq. (44) and the analogous CFL number C_A for various K_S, where C_A is defined as

$$C_A = \max_{0 \leqslant s \leqslant L} (\sqrt{T/\rho_1}\Delta t/\Delta s). \tag{45}$$

Here $\sqrt{T/\rho_1}$ denotes the speed of waves traveling along the filament. We can see that a small stretching coefficient ($K_S = 100$) is not acceptable due to large length error ($\varepsilon = 0.38$), while a too large value ($K_S = 10{,}000$) leads to a stiff system (maximum $\Delta t = 0.0001$ and $C_A = 0.044$). Using the present formulation, i.e. the inextensibility condition, the simulations were carried out at the same time steps as those of various K_S, as shown in Table 2. The length error is well controlled even for the largest time step used in this simulation ($\Delta t = 0.001$) and the corresponding C_A is 0.31. The computation is always stable for $\gamma = 0$ using the present method. However, numerical instability is invoked when increasing γ because the bending force term is calculated explicitly. Table 3 displays the maximum time step, the length error and the analogous CFL number for various γ and N. It is shown that the maximum time step decreases as γ increases or N increases. Since we only deal with very soft filaments, i.e. with small γ, the numerical instability limitation due to the bending force term is not significant.

4.2. A flexible filament flapping in a uniform fluid flow

When a flexible filament is placed in a uniform flow, the computational domain is $-2 \leqslant x \leqslant 6$ and $-4 \leqslant y \leqslant 4$, where these dimensions are scaled by L_r. Two different lengths ($L = 1$ and $L = 0.5$) are tested

Table 2
Comparison of the length error (ε) and the analogous CFL number (C_A) of the extensible case at the maximum time step (Δt) with those of the inextensible case at the same time step

K_S	Δt	ε	C_A
10^2	1.0×10^{-3}	0.38	0.42
10^3	3.1×10^{-4}	0.040	0.14
10^4	1.0×10^{-4}	0.0040	0.044
Inextensible	1.0×10^{-3}	2.0×10^{-8}	0.31
	3.1×10^{-4}	3.3×10^{-10}	0.097
	1.0×10^{-4}	4.4×10^{-12}	0.031

Table 3
The maximum time step (Δt), the length error (ε) and the analogous CFL number (C_A) of the inextensible case for different bending coefficient (γ) and node number (N)

	γ	Δt	ε	C_A
$N = 64$	10^{-4}	8.1×10^{-3}	1.6×10^{-6}	1.59
	10^{-3}	2.3×10^{-3}	1.3×10^{-8}	0.45
	10^{-2}	7.3×10^{-4}	1.1×10^{-10}	0.14
$N = 100$	10^{-4}	3.0×10^{-3}	1.1×10^{-7}	0.94
	10^{-3}	9.2×10^{-4}	6.1×10^{-10}	0.29
	10^{-2}	2.8×10^{-4}	6.0×10^{-12}	0.088

in the present simulations, using a grid size of 513×251 in the streamwise and transverse directions, respectively. The grid is uniformly distributed in the streamwise direction. In the transverse direction, however, the grid is uniformly distributed in $-1 \leqslant y \leqslant 1$ but stretched outside. Other computational parameters are $\alpha = -10^5$, $\beta = -10^2$ and $\Delta t = 0.0002$.

For $Re = 200$ and $\gamma = 0.001$, the instantaneous vorticity contours over a filament are shown in Fig. 8 at four instants that approximately span a flapping period, $t = 9.2$, 10.0, 10.8 and 11.6. Other parameters $\rho = 1.5$, $Fr = 0.5$, $L = 1$ and $N = 64$ are unchanged in this simulation. *BC1* (Eq. (9)) is applied at the fixed end and $k = 0.1\pi$ for the initial condition (Eq. (43)), which is large enough to achieve a self-sustained flapping state. Symmetric vortices are shed alternately from the flexible filament at the moment when it is most bent. Fig. 9 shows the instantaneous vorticity contours at $Re = 200$ for a more flexible filament ($\gamma = 0.0001$). This filament bends to a greater degree at the free end compared to the $\gamma = 0.001$ filament in Fig. 8. As a result, each vortex shedding from the filament tends to be split into two, although the two small vortices do not completely separate. For $Re = 500$ and $\gamma = 0.0001$ (Fig. 10), two positive and two negative vortices are shed sequentially from the filament. Again, in this system each vortex is split into two small vortices by the bending of the free end. Interestingly, a previous study of the flow around a swimming eel also observed that two same-sign vortices were shed per tail beat [30,31]. For $Re = 1000$ and $\gamma = 0.0001$ (see Fig. 11), the vortex structure becomes smaller, and the number of small vortices of each sign in one shedding period is increased to three. The trend in the flow pattern with increasing Reynolds number is consistent with the experimental results of Zhang et al. [1], which showed that a procession of small vortices is produced at high Reynolds number (about

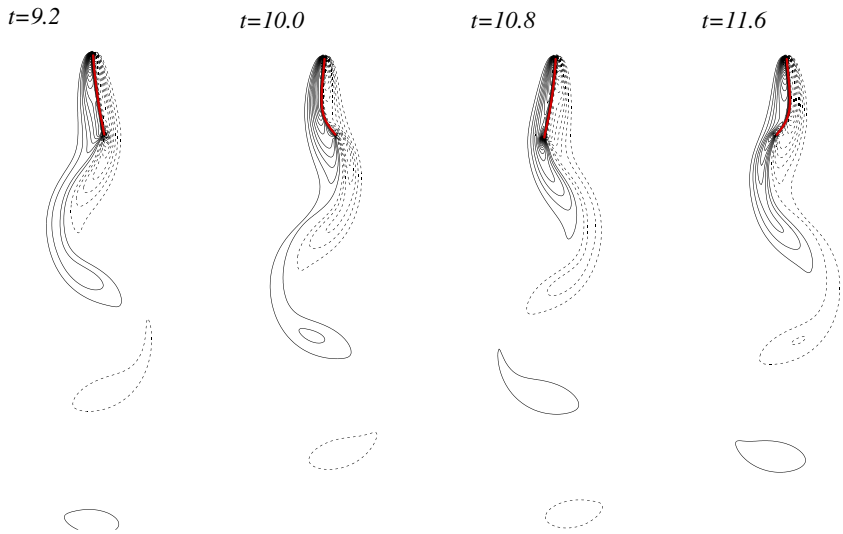

Fig. 8. Instantaneous vorticity contours of a uniform flow over a filament at $Re = 200$ and $\gamma = 0.001$ at four successive times. Other parameters are $\rho = 1.5$, $Fr = 0.5$, $L = 1$, $N = 64$ and $k = 0.1\pi$. The position of the filament is denoted by the thick solid line. Positive vorticity is indicated by black solid lines with increment 1.0, while negative vorticity is indicated by black dotted lines with increment -1.0.

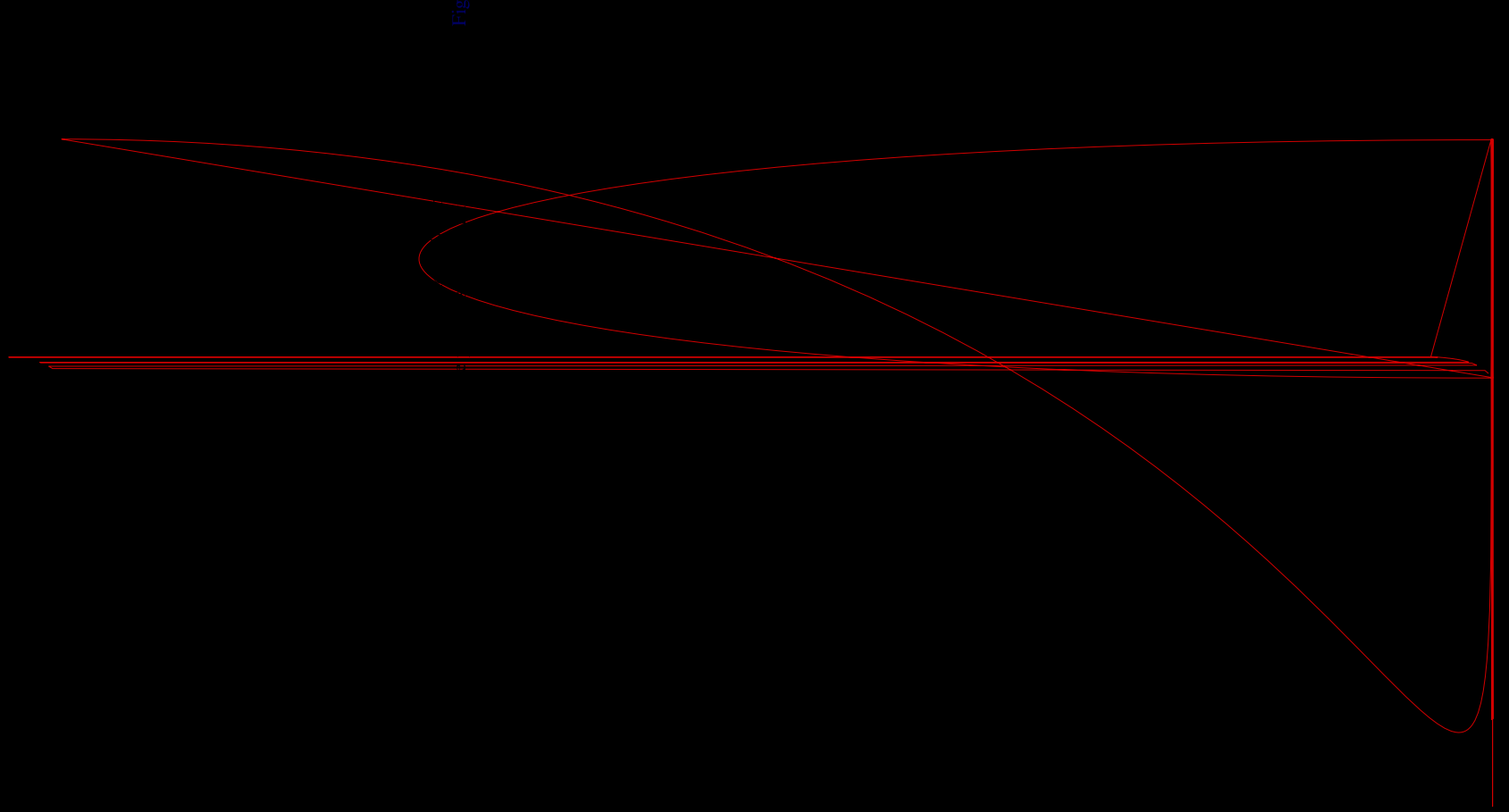

$$-\alpha\Delta t^2 - 2\beta\Delta t < C_T, \tag{46}$$

where C_T is a constant obtained from ρ, Δs, the type of smoothed delta function, and the time marching scheme of the flow solver. By substituting the values of α, β and Δt in Table 4 into Eq. (46), we obtain $C_T \approx 0.17$. For $\gamma = 0.001$, the maximum time step is also determined by α and β when $-\alpha \geqslant 10^4$ and $-\beta \geqslant 10^2$, which is the same as that of $\gamma = 0.0001$. When $\alpha = -10^4$ and $\beta = -10$, however, the maximum time step is determined by the stability arising from the filament computation ($\Delta t = 0.0023$ in Tables 3 and 4).

Convergence test was carried out for various α, β and Δt, as shown in Fig. 13. The curves collapse well for $-\alpha \geqslant 10^5$ at both $\Delta t = 0.0003$ and $\Delta t = 0.0006$, but deviate slightly as time goes by for $\alpha = -10^4$. β plays an insignificant role in convergence. Convergence test for node number N was carried out for $\gamma = 0$ since the bending force varies with N significantly. As shown in Fig. 14, the difference among the curves of $N = 56$, 64 and 72 is negligible, while the curve of $N = 48$ shows a slight deviation from others.

To study the bistable property of the present system, we consider both $L = 1$ and $L = 0.5$. The node numbers along the filament (N) for these systems are 64 and 32, respectively, and other parameters used are $Re = 300$, $\gamma = 0.001$, $\rho = 1.0$ and $Fr = 0.5$. The behaviors of filaments with *BC1* and *BC2* boundary conditions at the fixed end ($s = L$) are compared. Note that the initial condition given by Eq. (43) is not consistent with *BC2* due to the value of $\partial\vec{X}/\partial s$ at the fixed end. Hence we use another initial condition

$$\boldsymbol{X}_{i-1} = \boldsymbol{X}_i + (\Delta s\cos(N-i)a, \Delta s\sin(N-i)a), \quad \boldsymbol{U}_{i-1} = (0,0), \quad i = N, N-1, \ldots, 1 \tag{47}$$

for both *BC1* and *BC2* in these simulations, where a is a small constant.

Fig. 15 shows the influence of filament length and boundary condition on the bistable property of the system. For the short filament ($L = 0.5$; Fig. 15(a)), by setting a large initial disturbance $a = 0.03$ in Eq. (47) (initially the free end is located at $\boldsymbol{X}_0 = (0.43, 0.22)$), self-sustained flapping eventually develops for both *BC1* and *BC2*, although the filament with *BC2* requires a longer time to reach the equilibrium state. The amplitude of oscillation at the equilibrium state is slightly smaller for *BC2* than for *BC1*, while the flapping frequency is slightly higher for *BC2* because more energy is stored at the fixed end under this boundary condition. On the other hand, by setting a small value of $a = 0.01$ (initially $\boldsymbol{X}_0 = (0.49, 0.08)$), the initial disturbance decays gradually and the filament comes to rest at the stretched-straight state. For a small initial disturbance, the motion is mostly limited to the region close to the free end; hence there is little difference between *BC1* and *BC2* in Fig. 15(a) when the motion is decaying. The instantaneous vorticity contours are shown in Fig. 16 for $L = 0.5$ with *BC1*. In these maps, the bistable property is clearly seen with different initial disturbances. For $a = 0.01$ (Fig. 16(a)), the filament is in its stable stretched-straight state, like a rigid plate, and the vorticity contour is symmetric about the filament. For $a = 0.03$ (Fig. 16(b)), however, the filament is in its self-sustained flapping state, and vortices are shed alternately.

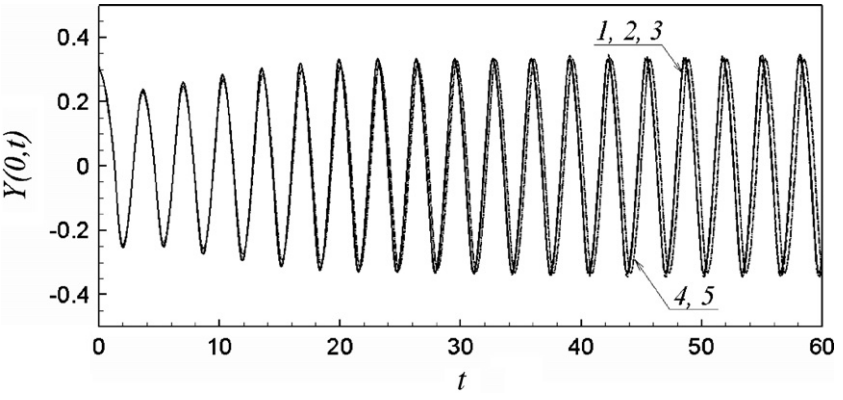

Fig. 13. Time history of the free end position of the filament at $Re = 200$, $\gamma = 0.001$, $\rho = 1.5$, $Fr = 0.5$, $L = 1$, $N = 64$ and $k = 0.1\pi$. Line 1: ——, $\alpha = -10^6$, $\beta = -10^2$, $\Delta t = 0.0003$; Line 2: ---, $\alpha = -10^5$, $\beta = -10^2$, $\Delta t = 0.0003$; Line 3: - - - -, $\alpha = -10^5$, $\beta = -10^2$, $\Delta t = 0.0006$; Line 4: ....., $\alpha = -10^4$, $\beta = -10^2$, $\Delta t = 0.0006$; Line 5: -·-·-, $\alpha = -10^4$, $\beta = -10^1$, $\Delta t = 0.0006$.

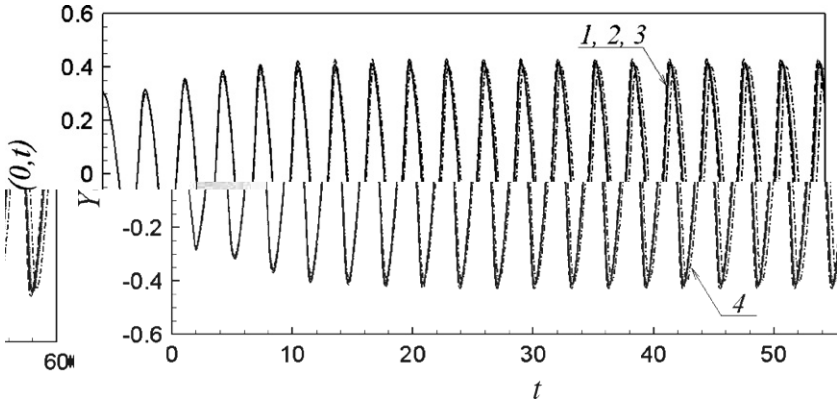

Fig. 14. Time history of the free end position of the filament at $Re = 200$, $\gamma = 0$, $\rho = 1.5$, $Fr = 0.5$, $L = 1$ and $k = 0.1\pi$. Line 1: ——, $N = 72$, Line 2: ---, $N = 64$; Line 3: ....., $N = 56$; Line 4: -·-·-·, $N = 48$.

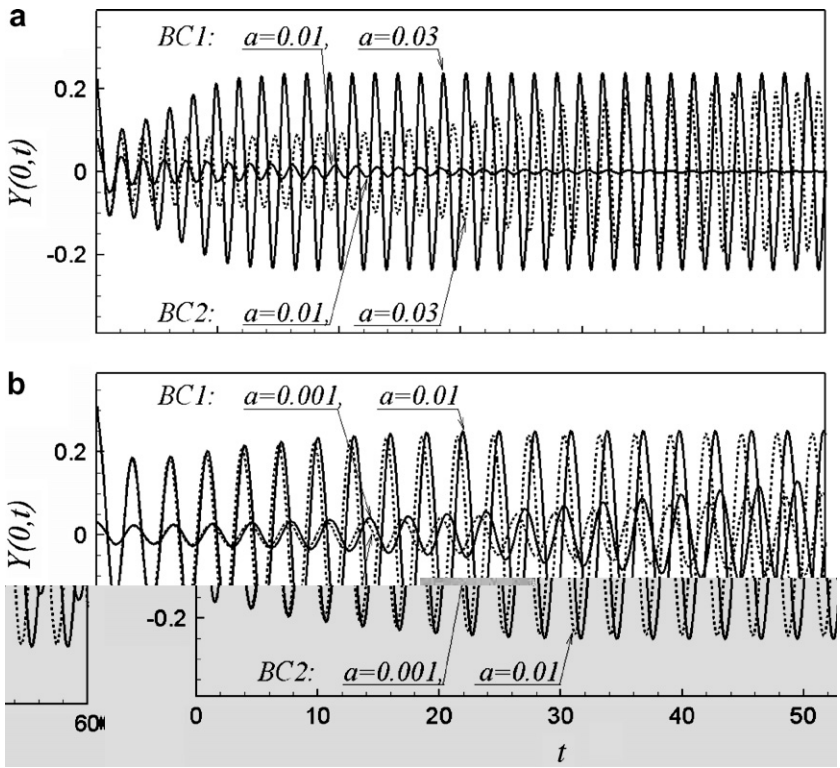

Fig. 15. Time history of the free end position of the filament with (a) $L = 0.5$ and $N = 32$; (b) $L = 1.0$ and $N = 64$. Other parameters are $\gamma = 0.001$, $\rho = 1.0$, $Fr = 0.5$ and $Re = 300$. $BC1$ is represented by a solid line and $BC2$ by a dashed line.

For the longer filament ($L = 1$; Fig. 15(b)), a self-sustained flapping state quickly develops for both *BC1* and *BC2* with an initial disturbance $a = 0.01$ (initially $\boldsymbol{X}_0 = (0.93, 0.31)$), and slowly develops for a small initial disturbance $a = 0.001$ (initially $\boldsymbol{X}_0 = (0.999, 0.032)$). In all of our simulations of filaments of length $L = 1$, the flapping state eventually developed no matter how small the initial disturbance. This is consistent with the experimental finding that the stable stretched-straight state disappears and only the flapping state remains if L is sufficiently large [1].

Fig. 8

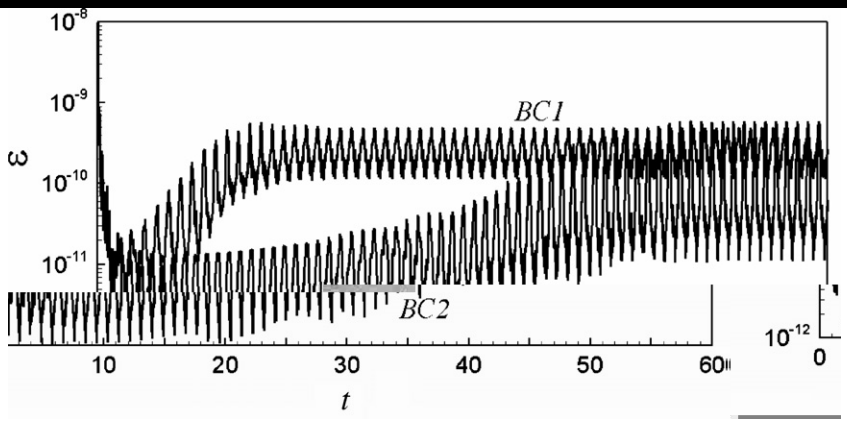

Fig. 17. Time history of the error of the inextensibility constraint of the filament at $Re = 150$, $\gamma = 0.001$, $\rho = 1.0$, $Fr = 0.5$, $L = 0.5$, $N = 32$ and $a = 0.03$.

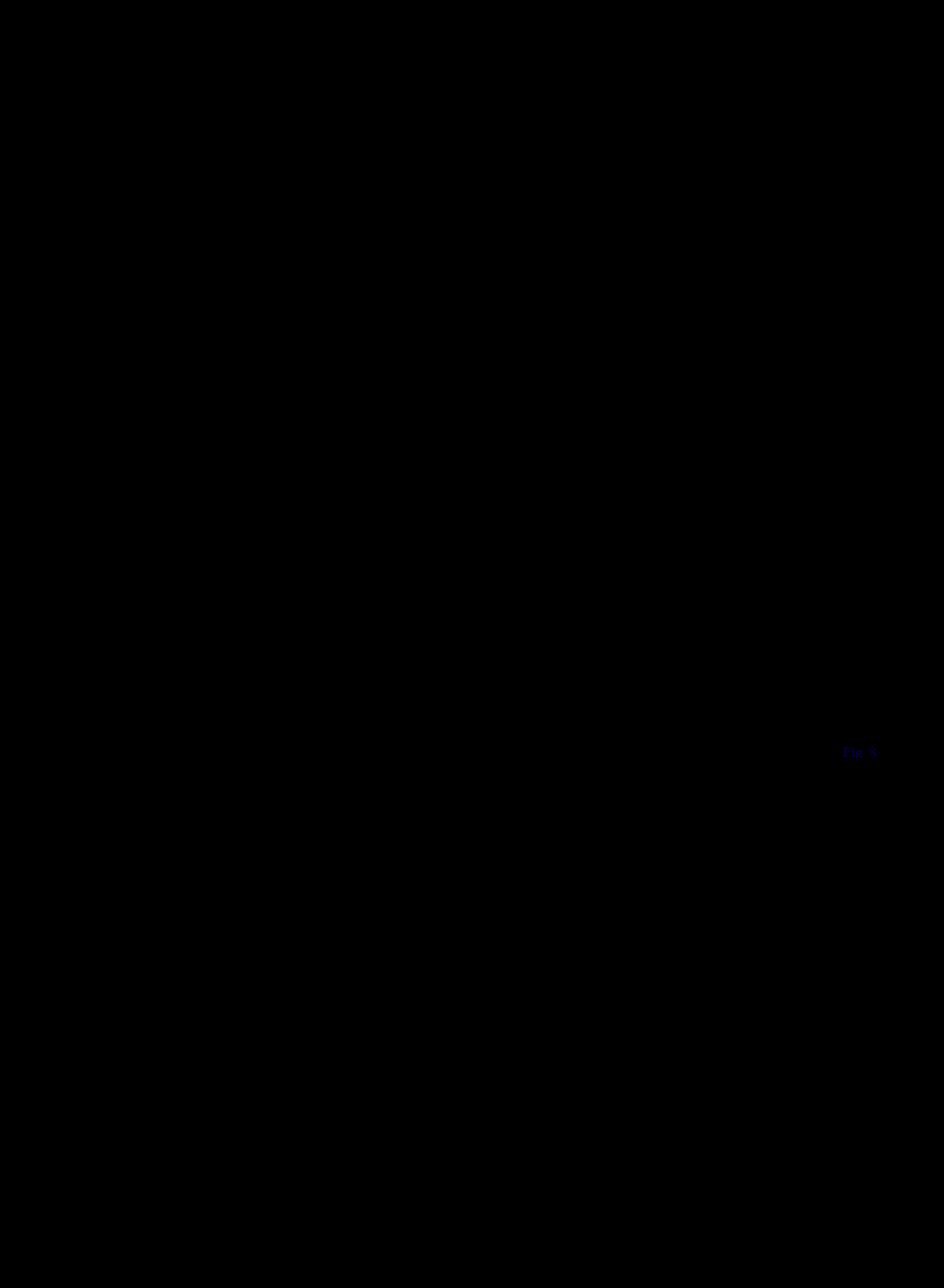

Fig. 8

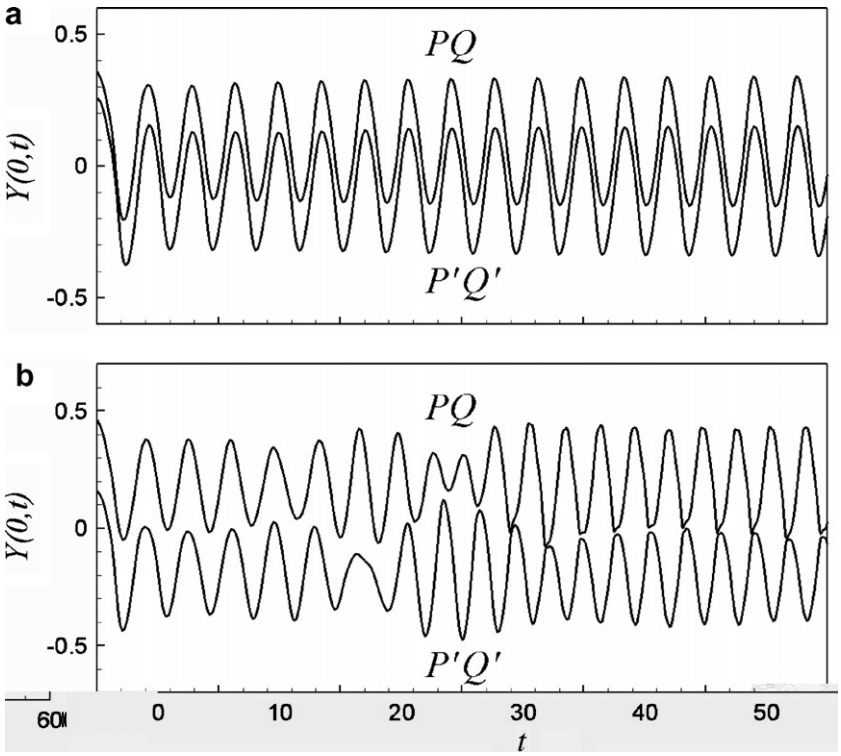

Fig. 20. Time history of the free end positions of both filaments for (a) $d = 0.1$; (b) $d = 1.0$. Other parameters are $Re = 300$, $\gamma = 0.001$, $\rho = 1.5$, $Fr = 0.5$, $L = 0.3$, $N = 64$ and $k = 0.1\pi$.

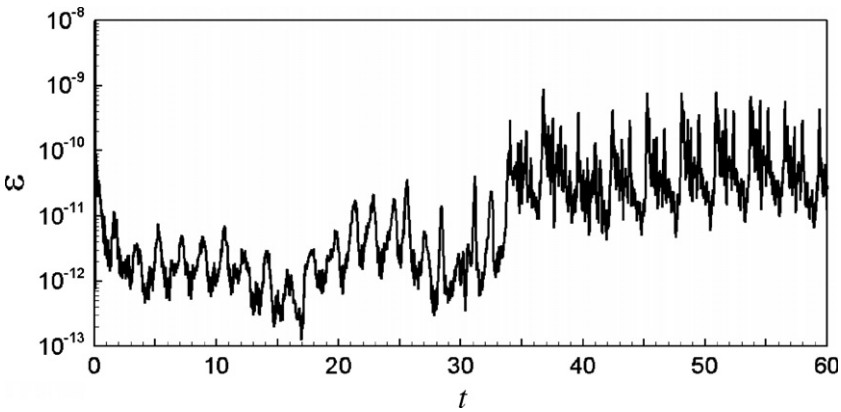

Fig. 21. Time history of the error of the inextensibility constraint of both filaments for $d = 0.3$. Other parameters are $Re = 300$, $\gamma = 0.001$, $\rho = 1.5$, $Fr = 0.5$, $L = 1$, $N = 64$ and $k = 0.1\pi$.

system. In the present formulation, the fluid motion defined on a Eulerian grid and the filament motion defined on a Lagrangian grid were solved independently and their interaction force was calculated explicitly via a feedback law. The governing equations were non-dimensionalized and the transformation between the Eulerian and Lagrangian variables was established using the Dirac delta function. A direct numerical method was developed to calculate the filament motion under the inextensibility condition. The stability limitation caused by the large stretching coefficient to approximate the inextensibility condition was relaxed by the present algorithm. A swinging filament resembling a rope pendulum was simulated with and without a bending force, and kicking was observed only for the flexible filament without a bending force. The error of the inex-

tensibility constraint was well controlled. In the case of small amplitude swinging without the bending force, the numerical result was in excellent agreement with the analytical solution derived by the perturbation method. A flexible filament in a uniform flow was simulated at different Reynolds numbers and bending rigidities. It was found that the maximum time step is determined by the stability arising from either the feedback forcing or the filament itself. The results showed that the production of small vortex processions was a combined effect of Reynolds number and bending rigidity. The bistable property of the system was observed for the filament of length $L = 0.5$ for both simply supported and clamped conditions at the fixed end, whereas only the stable flapping state was observed at $L = 1.0$. At the self-sustained flapping state, with the clamped condition at the fixed end, the flapping amplitude was smaller and the frequency was larger than the corresponding values with the simply-supported condition. Two side-by-side filaments in a uniform flow were then simulated at different inter-distances. In-phase and out-of-phase flappings were observed at $d = 0.1$ and 0.3, respectively. A short-range repulsive force, formulated using the Dirac delta function, was included in the formulation; this force was activated in the case of out-of-phase flapping when the free ends of the two filaments collided. The inextensibility condition was well satisfied in the present simulations.

Acknowledgements

This work was supported by the Creative Research Initiatives of the Korea Science & Engineering Foundation and partially supported by the Korea Institute of Science and Technology Information under the 8th Strategic Supercomputing Support Program.

Appendix

By assuming $\gamma = 0$, $\boldsymbol{F} = 0$ and $\boldsymbol{F}_c = 0$, the analytical solution of Eqs. (6) and (4) is derived here by the perturbation method for small-amplitude motion, subjected to the boundary conditions $|\boldsymbol{X}(0,t)| < \infty$ and $\boldsymbol{X}(L,t) = (0,0)$, and the initial conditions in Eq. (43). Let $\boldsymbol{X}_0(s) = (L - s, 0)$ and $T_0(s) = Fr \cdot s$ denote the resting state. The perturbation to the resting state is expressed by

$$\boldsymbol{X}(s,t) = \boldsymbol{X}_0(s) + \varepsilon \boldsymbol{X}_1(s,t) + \cdots \tag{48}$$

and

$$T(s,t) = T_0(s) + \varepsilon T_1(s,t) + \cdots, \tag{49}$$

where ε is a small positive number. Substituting Eq. (48) into Eq. (4) and neglecting the terms with ε^2, we obtain $\boldsymbol{X}_1(s,t) = 0$. Thus Eq. (6) and the corresponding boundary and initial conditions become

$$\frac{\partial^2 Y(s,t)}{\partial t^2} = \frac{\partial}{\partial s}\left(Fr \cdot s \frac{\partial Y(s,t)}{\partial s}\right), \tag{50}$$

$$Y(L,t) = 0, \quad |Y(0,t)| < \infty, \tag{51}$$

$$Y(s,0) = k(L-s), \quad \frac{\partial Y(s,0)}{\partial t} = 0. \tag{52}$$

Using the method of separation of variables, a series solution of the above boundary value problem (Eqs. (50) and (51)) has been found by Bailey [15]

$$Y(s,t) = \sum_{i=1}^{\infty} J_0\left(z_i\sqrt{\frac{s}{L}}\right)\left[A_i \cos\left(\frac{z_i t}{2}\sqrt{\frac{Fr}{L}}\right) + B_i \sin\left(\frac{z_i t}{2}\sqrt{\frac{Fr}{L}}\right)\right], \tag{53}$$

where J_0 is the Bessel function of the first kind of order zero, z_i is the ith positive root of $J_0(z)$, and A_i and B_i are free constants which are determined by the initial conditions. From the second condition of Eq. (52), we have $B_i = 0$, $i = 1, 2, \ldots$. The first condition in Eq. (52) is equivalent to

$$\sum_{i=1}^{\infty} A_i J_0\left(z_i\sqrt{\frac{s}{L}}\right) = k(L-s). \tag{54}$$

By multiplying both sides of Eq. (54) by $J_0(z_j\sqrt{s/L})$ and then integrating with respect to s from 0 to L, we obtain

$$\sum_{i=1}^{\infty} A_i \int_0^L J_0\left(z_i\sqrt{\frac{s}{L}}\right) J_0\left(z_j\sqrt{\frac{s}{L}}\right) \mathrm{d}s = \int_0^L k(L-s) J_0\left(z_j\sqrt{\frac{s}{L}}\right) \mathrm{d}s, \quad j = 1, 2, \ldots \tag{55}$$

Then, by letting $s = Lr^2$ and using the orthogonal property of J_0, Eq. (55) becomes

$$A_j \int_0^1 r J_0^2(z_j r)\mathrm{d}r = kL \int_0^1 (r - r^3) J_0(z_j r)\mathrm{d}r, \quad j = 1, 2, \ldots \tag{56}$$

Together with the equalities

$$\int_0^1 r J_0^2(z_j r)\mathrm{d}r = \frac{1}{2} J_1^2(z_j), \tag{57}$$

$$\int_0^1 r J_0(z_j r)\mathrm{d}r = \frac{J_1(z_j)}{z_j}, \tag{58}$$

$$\int_0^1 r^3 J_0(z_j r)\mathrm{d}r = \frac{J_1(z_j)}{z_j} - \frac{2J_2(z_j)}{z_j^2}, \tag{59}$$

where J_1 and J_2 are the Bessel functions of the first kind of order one and two, respectively. Eqs. (57) and (58) can be solved by integration by parts. Thus

$$A_j = \frac{4kL}{z_j^2} \frac{J_2(z_j)}{J_1^2(z_j)}, \quad j = 1, 2, \ldots \tag{60}$$

The series solution to Eqs. (50)–(52) is finally obtained

$$Y(s,t) = \sum_{i=1}^{\infty} \frac{4kL}{z_i^2} \frac{J_2(z_i)}{J_1^2(z_i)} J_0\left(z_i\sqrt{\frac{s}{L}}\right) \cos\left(\frac{z_i t}{2}\sqrt{\frac{Fr}{L}}\right). \tag{61}$$

References

[1] J. Zhang, S. Childress, A. Libchaber, M. Shelley, Flexible filaments in a flowing soap film as a model for one-dimensional flags in a two-dimensional wind, Nature 408 (2000) 835–839.
[2] G. Huber, Swimming in flat sea, Nature 408 (2000) 777–778.
[3] U.K. Müller, Fish'n flag, Science 302 (2003) 1511–1512.
[4] J.C. Liao, D.N. Beal, G.V. Lauder, M.S. Triantafyllou, Fish exploiting vortices decrease muscle activity, Science 302 (2003) 1566–1569.
[5] F.E. Fish, G.V. Lauder, Passive and active flow control by swimming fishes and mammals, Annu. Rev. Fluid Mech. 38 (2006) 193–224.
[6] L. Zhu, C.S. Peskin, Simulation of a flapping flexible filament in a flowing soap film by the immersed boundary method, J. Comput. Phys. 179 (2002) 452–468.
[7] L. Zhu, C.S. Peskin, Interaction of two flapping filaments in a flowing soap film, Phys. Fluids 15 (7) (2003) 1954–1960.
[8] Y. Kim, C.S. Peskin, Penalty immersed boundary method for an elastic boundary with mass, peprint, 2005.
[9] Z. Yu, A DLM/FD method for fluid/flexible-body interactions, J. Comput. Phys. 207 (2005) 1–27.
[10] R. Glowinski, T.-W. Pana, T.I. Hesla, D.D. Joseph, A distributed Lagrange multiplier/fictitious domain method for particulate flows, Int. J. Multiphase Flow 25 (1999) 755–794.
[11] D.J.J. Farnell, T. David, D.C. Barton, Numerical simulations of a filament in a flowing soap film, Int. J. Numer. Methods Fluids 44 (2004) 313–330.
[12] A.-K. Tornberg, M.J. Shelley, Simulating the dynamics and interactions of flexible fibers in Stokes flows, J. Comput. Phys. 196 (2004) 8–40.
[13] D. Qi, A new method for direct simulations of flexible filament suspensions in non-zero Reynolds number flows, Int. J. Numer. Methods Fluids 54 (2007) 103–118.
[14] A. Thess, O. Zikanov, A. Nepomnyashchy, Finite-time singularity in the vortex dynamics of a string, Phys. Rev. E 59 (3) (1999) 3637–3640.
[15] H. Bailey, Motion of a hanging chain after the free end is given an initial velocity, Am. J. Phys. 68 (8) (2000) 764–767.
[16] A. Belmonte, M.J. Shelley, S.T. Eldakar, C.H. Wiggins, Dynamic patterns and self-knotting of a driven hanging chain, Phys. Rev. Lett. 87 (11) (2001) 114301.

[17] R. Mittal, G. Iaccarino, Immersed boundary methods, Annu. Rev. Fluid Mech. 37 (2005) 239–261.
[18] C.S. Peskin, Numerical analysis of blood flow in the heart, J. Comput. Phys. 25 (1977) 220–252.
[19] C.S. Peskin, The immersed boundary method, Acta Numer. (2002) 479–517.
[20] D. Goldstein, R. Handler, L. Sirovich, Modeling a no-slip flow boundary with an external force field, J. Comput. Phys. 105 (1993) 354–366.
[21] E.M. Saiki, S. Biringen, Numerical simulation of a cylinder in uniform flow: application of a virtual boundary method, J. Comput. Phys. 123 (1996) 450–465.
[22] C. Lee, Stability characteristics of the virtual boundary method in three-dimensional applications, J. Comput. Phys. 184 (2003) 559–591.
[23] M.-C. Lai, C.S. Peskin, An immersed boundary method with formal second-order accuracy and reduced numerical viscosity, J. Comput. Phys. 160 (2000) 705–719.
[24] M. Uhlmann, An immersed boundary method with direct forcing for the simulation of particulate flows, J. Comput. Phys. 209 (2005) 448–476.
[25] C. Eloy, C. Souilliez, L. Schouveiler, Flutter of a rectangular plate, J. Fluids Struct. 23 (2007) 904–919.
[26] C.S. Peskin, B.F. Printz, Improved volume conservation in the computation of flows with immersed elastic boundaries, J. Comput. Phys. 105 (1993) 33–46.
[27] K. Kim, S.-J. Baek, H.J. Sung, An implicit velocity decoupling procedure for incompressible Navier–Stokes equations, Int. J. Numer. Methods Fluids 38 (2002) 125–138.
[28] E. Guilmineau, P. Queutey, A numerical simulation of vortex shedding from an oscillating circular cylinder, J. Fluids Struct. 16 (6) (2002) 773–794.
[29] D. Kim, H. Choi, Immersed boundary method for flow around an arbitrarily moving body, J. Comput. Phys. 212 (2006) 662–680.
[30] U.K. Müller, J. Smit, E.J. Stamhuis, J.J. Videler, How the body contribute to the wake in undulatory fish swimming: flow fields of a swimming eel (*Anguilla Anguilla*), J. Exp. Biol. 204 (2001) 2751–2762.
[31] E.D. Tytell, G.V. Lauder, The hydrodynamics of eel swimming I. Wake structure, J. Exp. Biol. 207 (2004) 1825–1841.